Database of storm-time equatorial ion temperatures in Earth's magnetosphere calculated from energetic neutral atom data

Amy M Keesee[1], Roxanne Marie Katus[2], Matthew Floyd[2], and Earl E. Scime[3]

[1]University of New Hampshire
[2]Eastern Michigan University
[3]West Virginia University

November 22, 2022

Abstract

Ion temperature is a key parameter that influences dynamics in the magnetosphere, such as particle transport and wave-particle interactions. Measurements of ion heating and energization yields information about phenomena such as magnetic reconnection, bursty bulk flows, and ion injections. Taking advantage of the global view provided by energetic neutral atom imaging, a database of ion temperature maps during geomagnetic storms occurring throughout the NASA TWINS mission has been created. These ion temperature maps and relevant metadata are publicly available on CDAWeb to facilitate comparison to in situ measurements and model output, for use as boundary conditions for simulations, and for other relevant studies. A preliminary study of average plasma sheet ion temperatures calculated from these maps has revealed a common occurrence of decreasing ion temperature concurrent with a sharp negative gradient in the IMF B. A preliminary case study for one storm is presented.

Database of storm-time equatorial ion temperatures in Earth's magnetosphere calculated from energetic neutral atom data

A. M. Keesee[1], R. M. Katus[2], M. Floyd[2], and E. E. Scime[3]

[1]Department of Physics & Astronomy and Space Science Center, University of New Hampshire, Durham, NH.

[2]Department of Mathematics, Eastern Michigan University, Ypsilanti, MI.

[3]Department of Physics & Astronomy, West Virginia University, Morgantown, WV.

Corresponding author: Amy Keesee (amy.keesee@unh.edu)

Key Points:

- Equatorial ion temperature maps have been calculated from ENA data at 10-minute time cadence for 2009-2017
- The database of temperature maps is available on CDAWeb
- A case study of ion temperature drops in the plasma sheet is presented

Abstract

Ion temperature is a key parameter that influences dynamics in the magnetosphere, such as particle transport and wave-particle interactions. Measurements of ion heating and energization yields information about phenomena such as magnetic reconnection, bursty bulk flows, and ion injections. Taking advantage of the global view provided by energetic neutral atom imaging, a database of ion temperature maps during geomagnetic storms occurring throughout the NASA TWINS mission has been created. These ion temperature maps and relevant metadata are publicly available on CDAWeb to facilitate comparison to in situ measurements and model output, for use as boundary conditions for simulations, and for other relevant studies. A preliminary study of average plasma sheet ion temperatures calculated from these maps has revealed a common occurrence of decreasing ion temperature concurrent with a sharp negative gradient in the IMF B_Z. A preliminary case study for one storm is presented.

Plain Language Summary

The Sun releases large chunks of energetic particles that can bombard the region of space surrounding Earth, causing an event called a geomagnetic storm. During these storms, particles can become heated and move around. We can measure the temperature of these particles to improve our understanding of what happens during these storms. We have made maps of such temperatures and are sharing them publicly so that others can use them in their own research. We have found some cases where the average temperature of space on the night-side of Earth decreases rapidly and remains low. This could be controlled by the magnetic field embedded in the chunks of energetic particles coming from the Sun, but a more detailed study is needed to find out.

1 Introduction

The terrestrial magnetosphere contains several distinct plasma populations: the plasmasphere, the ring current, the ionosphere, the radiation belts, and the plasma sheet. The plasma sheet is a layer of hot plasma that extends from the magnetotail into the inner magnetosphere. This region plays an important role in the transfer of energy from the solar wind to the Earth. The ion population in the plasma sheet influences the dynamics of the inner magnetosphere, especially during geomagnetically active intervals. Ions are convected or injected into the inner magnetosphere where they drive the ring current as well as waves that excite radiation belt particles (Ozeke & Mann, 2008; Takahashi, Seki, Amano, Miyoshi, & Yamakawa, 2019). Because of this, ion densities and temperatures are needed as boundary conditions for inner magnetosphere models.

Borovsky et al. (1998) demonstrated a correlation between solar wind speed and ion temperature in the plasma sheet; and recent studies showed a similar correlation between solar wind speed and enhancement of MeV electrons in the radiation belt (Zhao, Baker, Li, Jaynes, & Kanekal, 2019). The Tsyganenko & Mukai (2003) plasma sheet models are statistical models based on long-time averages of Geotail data that lack event-specific spatial and temporal variation (Elfritz, Keesee, Buzulukova, Fok, & Scime, 2014). Ion heating in the plasma sheet is associated with numerous phenomena including gradient-curvature drift (Spence & Kivelson, 1993), adiabatic heating, magnetic reconnection, and bursty bulk flows (BBF) (Angelopoulos, Kennel, Kivelson, Walker, & Paschmann, 1992). Current modeling of the inner magnetosphere often involves coupling with a global magnetohydrodynamics (MHD) model. While these global models now have the ability to include transient events such as BBFs (e.g. Wiltberger, Merkin, Lyon, & Ohtani, 2015), it is unclear how well the temporal and spatial variation of the actual events are accurately modeled. Energetic neutral atom (ENA) imaging can provide a global view of the ion population to provide validation for MHD model results or be used directly for ion boundary conditions (Chen et al., 2015; Elfritz et al., 2014).

A dataset of ion temperature maps created from TWINS ENA measurements for storms over July 2009 - July 2015 was previously made available through NASA Space Physics Data Facility (SPDF) and described in Keesee & Scime (2015). However, that dataset was provided as IDL savesets without complete metadata, limiting its usability. We have expanded and improved upon that database. We now include all moderate and intense storms (Dst ≤ -60 nT) during July 2009-December 2017, increased the time cadence of the temperature maps to 10 minute averages, and increased the total interval analyzed for each storm to include four days, with the storm peak on the second day. This ensures that there is plenty of prestorm data, the entire main phase - the average main phase is 13.7 hours (Roxanne M Katus, Liemohn, Ionides, Ilie, & Welling, 2015)-, and two days of recovery. The new database is provided in Common Data Format (CDF) with critical metadata to make the dataset more readily available for use. Also included are arrays of the equatorial ENA flux used to calculate the ion temperatures. The dataset is archived at the NASA SPDF CDAWeb in a format compatible with the Virtual Observatory (VxO) architecture. In Section 2, we describe the TWINS ENA data, ion temperature calculation methodology, storms included in the database, and provide a user guide for the database. In Section 3 we provide an example analysis of the data including a detailed description of some of the nuances of the ion temperature maps.

2 Ion Temperature Database

2.1 TWINS Data and Ion Temperature Calculation

The Two Wide-angle Imaging Neutral atom Spectrometers (TWINS) is a NASA Mission of Opportunity (McComas et al., 2009). TWINS is housed on two satellites in highly elliptical Molniya orbits with perigee of ~7 R_E that are alternating to provide near-continuous coverage. Each satellite contains an energetic neutral atom (ENA) imager, a Lyman-alpha detector, and in situ particle monitors. The ENA imagers are placed on actuators to provide two-dimensional, time-of-flight measurements. Additional details are available elsewhere (Goldstein & McComas, 2013, 2018; A M Keesee, Chen, Scime, & Lui, 2014).

Two-dimensional ion temperature maps (e.g., Figure 1a) were created using the methods of ion temperature calculation and line-of-sight (LOS) projection that have been previously validated with in situ measurements (A. Keesee, Scime, Zaniewski, & Katus, 2019; A M Keesee et al., 2014; A M. Keesee, Scime, & Moldwin, 2008; Scime et al., 2002). Once the ENA flux and orbit data were obtained as a function of date and spacecraft, two procedures were implemented to maintain data quality. The first procedure removed all intervals with an actuator pointing uncertainty above 4°. Second, intervals when the instrument was facing the sun were removed. As described previously, the ENA flux is projected to a 160 × 160 grid with 0.5 R_E resolution extending from -60 R_E to 20 R_E in the x-direction and -40 R_E to 40 R_E in the y-direction using

GSM coordinates (A. M. Keesee, Elfritz, McComas, & Scime, 2012). Note that this projection yields decreasing spatial resolution with increasing distance from Earth.

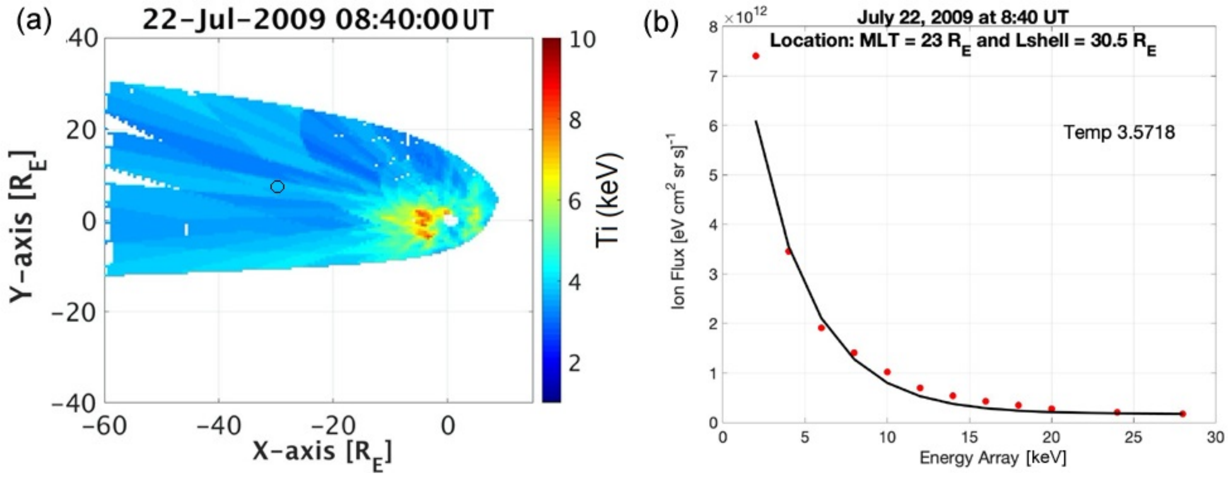

Figure 1. (a) Magnetospheric ion temperature data mapped to the equatorial plane for July 22, 2009 at 8:40 UT. The Sun is to the right and dawn is down. (b) Ion flux versus energy (circles) and a fit to the data (solid line) using Eq. (1) at x = – 30 R_E and y = 7 R_E, resulting in a temperature of 3.6 keV.

The projected ENA flux is converted to ion differential flux and fit to the equation,

$$\frac{J_{ENA}}{\sigma_{cx}(E)E} \approx \frac{C}{\left(\pi T_i(r)\right)^{3/2}} exp\left(\frac{-E}{T_i(r)}\right) \qquad (1)$$

to calculate the ion temperature at each grid location, where $J_{ENA}$is ENA flux, $\sigma_{cx}$is the energy-dependent charge exchange cross section, E is the energy, C is a constant, and $T_i(r)$is the ion temperature at location r. An example ion flux spectrum and fit of Eq. 1 is shown in Figure 1b. This method assumes all ENAs are hydrogen, a Maxwellian parent ion distribution, negligible collisions between the charge-exchange collision that creates the ENA and detection by the instrument, and that the hottest point along the LOS lies in the equatorial plane. For parent ion populations that are not Maxwellian, the "temperature" shows the amount of energization of the bulk population. Contributions from oxygen ENAs increase the flux values in the low energy (< 5 keV) bins as is evident in Figure 1b. Errors in the ion temperatures calculated using this method have been shown to be < 3 keV through comparison to in situ measurements (R. M. Katus, Keesee, Scime, & Liemohn, 2017).

2.2 Storm Selection

The geomagnetic storms available in the database include all that are of at least moderate intensity during the lifetime of the TWINS mission (July 2009-December 2017). They were selected using the Disturbance storm time (Dst) index from the Kyoto database with minimum Dst ≤ -60 nT. TWINS data with a 10-minute time cadence over a four-day window (starting the day prior to the day on which the minimum Dst occurred) were analyzed to provide pre-storm conditions as well as complete coverage of the main and recovery phases of the storm. A table of storms is provided in the supplemental material.

2.3 Database User Guide

The data are converted to CDF with all descriptions and metadata in Extensible Markup Language (XML) according to the Space Physics Archive Search Model. The metadata include the date, time, the spacecraft position, and the name (TWINS-1 or TWINS-2) of the satellite used to produce the time step.

To access the data on CDAWeb (https://cdaweb.gsfc.nasa.gov/index.html/), select "TWINS" from the Source column and click "Submit." Select "TWINS_M2_ENA" and click "Submit." When selecting Start and Stop times, refer to the table of storms in the supplemental material of this article. Three variable parameters are available. 1. The "Inner Magnetospheric Ion Temperature images" plots all 10-minute interval maps that are available within the selected time range. Clicking on an individual map opens it up in a separate window. 2. "Movie display" creates an Animated GIF and MP4 movie of the individual images. 3. "TWINS Satellite 1 or 2 Used to calculate the Ion Temperature" provides a line plot indicating the satellite used for each interval. An array of the data can be obtained by using "List Data," which will be given as ion temperature values in keV as a function of x and y location in R_E for each interval. Grid locations that do not have a temperature value (e.g. outside of the magnetosphere boundary) are set to -1.0. Users are encouraged to read the example analysis below as well as our prior publications to gain an understanding of the nuances of the data.

3 Example analysis

To demonstrate the utility of the database, we have conducted a preliminary analysis of the average plasma sheet ion temperature during storm time evolution as a function of solar wind parameters. The average plasma sheet ion temperature is calculated by selecting the region $-60\ R_E < x < -5\ R_E$ and 20:00 < MLT < 4:00 from the 10-minute averaged temperature maps, shown in Figure 2a. Using MLT results in varying coverage along the y-axis that increases with distance from the Earth, with $-10\ R_E < y < 10\ R_E$ at geosynchronous orbit. Figure 2b shows the average ion temperatures for July 21-25, 2009, with the average from the individual satellites shown in the 2nd and 3rd panels. Those values are also shown in the first panel in blue for TWINS 1 and red for TWINS 2, with the final calculated average in yellow. When data from only one satellite is available, the average plasma sheet ion temperature from that satellite is used for the final average. When there are overlapping intervals between the two TWINS satellites, an average map is first created by calculating the average temperature in each equatorial plane bin from the individual satellite maps, then the average over the plasma sheet region from the average map is calculated. Note that if one satellite has a larger FOV, the equatorial plane bins that are only populated in the map for that satellite will take on the value from that satellite in the average map, thus it will have more weight in the plasma sheet average. This can be seen when considering the interval on July 22, 2009 from 00:00 UT to 1:40 UT. In the top panel of Figure

2b, the yellow final average lies closer to the red TWINS 2 average than the blue TWINS 1 average. The ion temperature maps from four of the 10-minute averages during this interval are shown in Figure 2c, with the rows showing the maps for TWINS 1, TWINS 2, and the averaged map, respectively. It can be seen that the larger FOV of TWINS 2 during this interval contributes more bins to the plasma sheet area than TWINS 1, so the final average (yellow in Fig. 2b) is dominated by contributions from TWINS 2 and will, therefore, be closer to the average calculated from the TWINS 2 map (red in Fig. 2b). This comparison, thus, gives some quantification of the error of the average ion temperature, which tends to be less than +/- 2 keV.

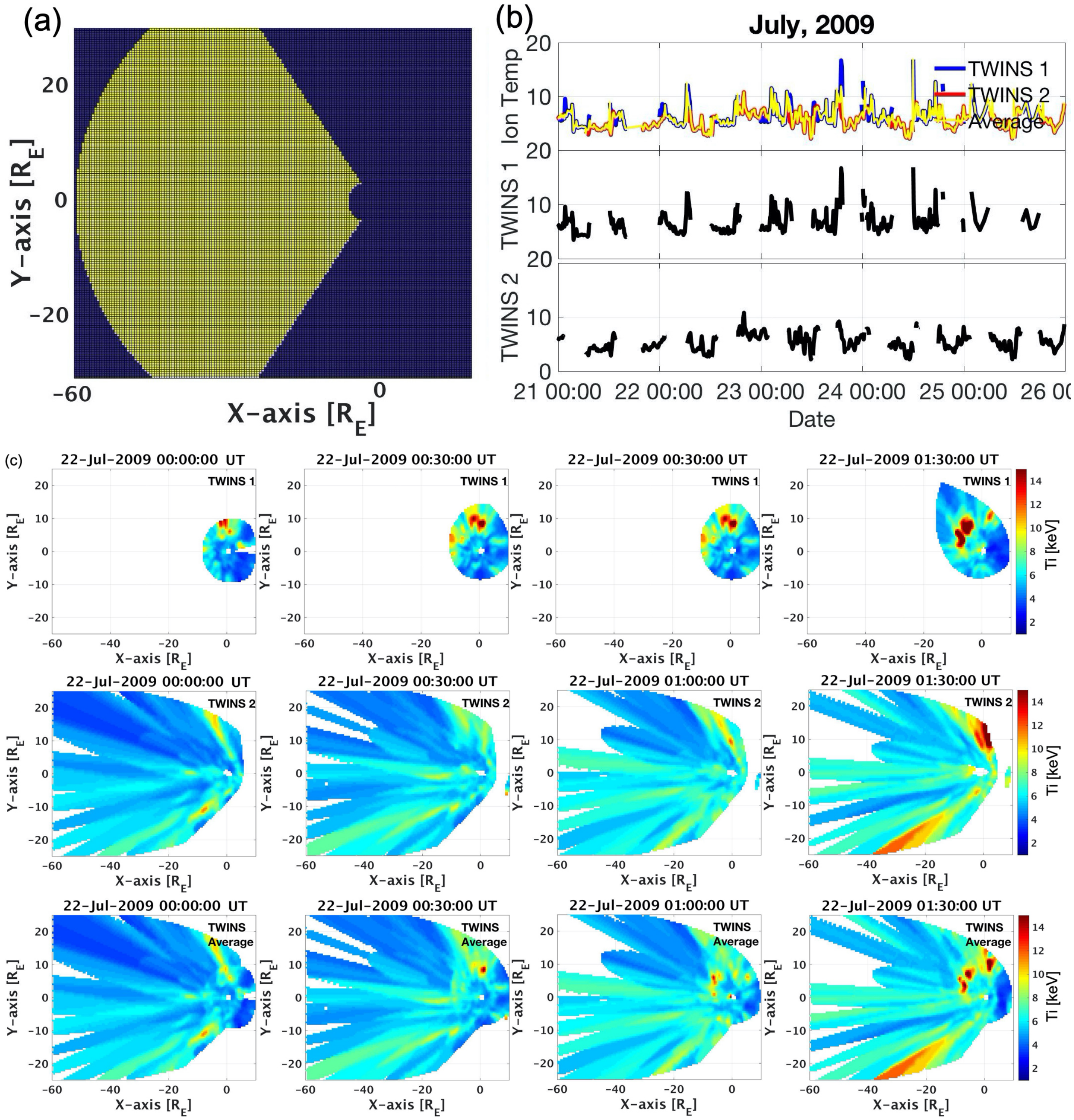

Figure 2. Calculation of the average plasma sheet ion temperature. a) The plasma sheet region used to calculate the ion temperature average is shown in yellow. b) Average ion temperature in the plasma sheet calculated from TWINS 1 (blue in top panel and second panel) and TWINS 2 (red in top panel and third panel) and the final average (yellow in top panel) that is calculated from an averaged map for overlapping intervals. c) Four 10-minute averages (columns) during an overlapping interval with the TWINS 1 (top row), TWINS 2 (middle row), and averaged map (bottom row) shown.

The 10-minute averages of solar wind dynamic pressure, IMF, velocity magnitude, AE, and Dst are obtained from OmniWeb for comparison. Using these data, we have found several cases where the plasma sheet temperature drops following a strong southward gradient in the IMF B_z, and the temperature remains low until the B_z recovers. One case study is described here.

During the July 22, 2009 storm there are two ion temperature drops associated with negative IMF B_z gradients. Figure 3 shows the average plasma sheet ion temperature along with IMF and solar wind conditions and the AE and Dst indices. The 10-minute averaged ion temperature maps are shown at 30-minute intervals in Figure 4 for 3:30-13:00 UT on July 22. The ion temperature increases over 5:00-6:30 UT on July 22nd, near the peak of the storm, following an increase in pressure and concurrent with a northward turning and increase in B_z. The temperature drops around 8:00 UT concurrent with a strong southward B_z turning. B_z returns northward around 9:00 UT, followed by a smaller ion temperature increase. The B_z turns southward again around 10:00 UT, followed by a second drop in the plasma sheet temperature that remains low for a couple of hours. The first southward B_z turning results in a large southward B_z compared to a much smaller magnitude for the second turning, but the average temperature is lower in the second interval which has a stronger B_z gradient. It can be seen in Figure 4 that there is a region of ~6 keV ions in the plasma sheet near the Earth during the first low temperature interval (Figs. 4j-m), but barely any enhanced regions in the second (Figs. 4o-s), resulting in that lower average temperature. A peak in the AE index following the large southward B_z turning around 8:00 UT indicates substorm activity and the Dst index has a second dip following this time as well. Thus, the first southward turning appears to have resulted in injections from the plasma sheet to the inner magnetosphere. The short northward turning only allowed for partial recovery and heating of the plasma sheet prior to the second, smaller southward B_z turning. The ion temperature returned to average values of ~ 5 keV around 13:00 UT after the B_z had been near zero for several hours.

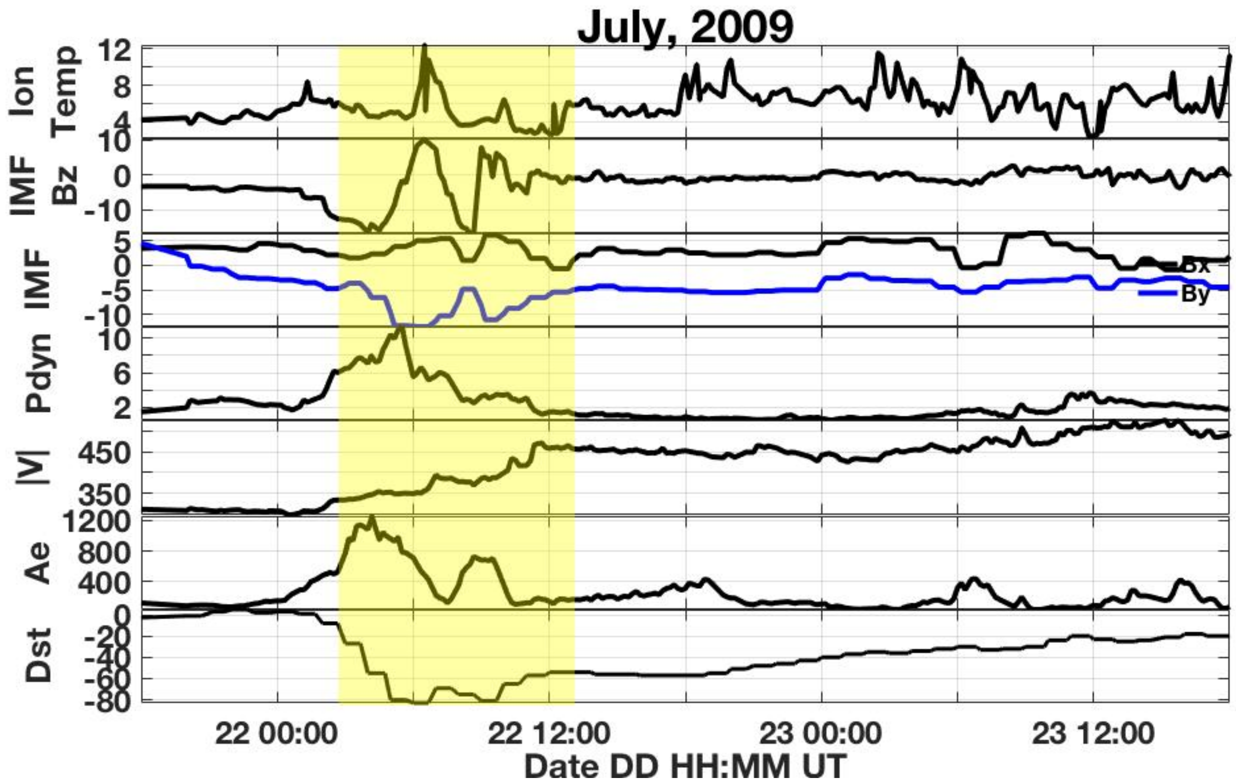

Figure 3. TWINS-derived spatially-averaged plasma sheet ion temperature at 10-minute averaged intervals (keV), and OMNIWeb obtained values averaged at 10-minute intervals of IMF B_z (nT), B_x (nT), B_y (nT), dynamic Pressure (nPa), velocity magnitude (km/s), AE index (nT), and Dst index (nT) as a function of time for July 21-23, 2009. The shaded area indicates the interval of interest, 3:30 UT-13:00 UT, as described in the text.

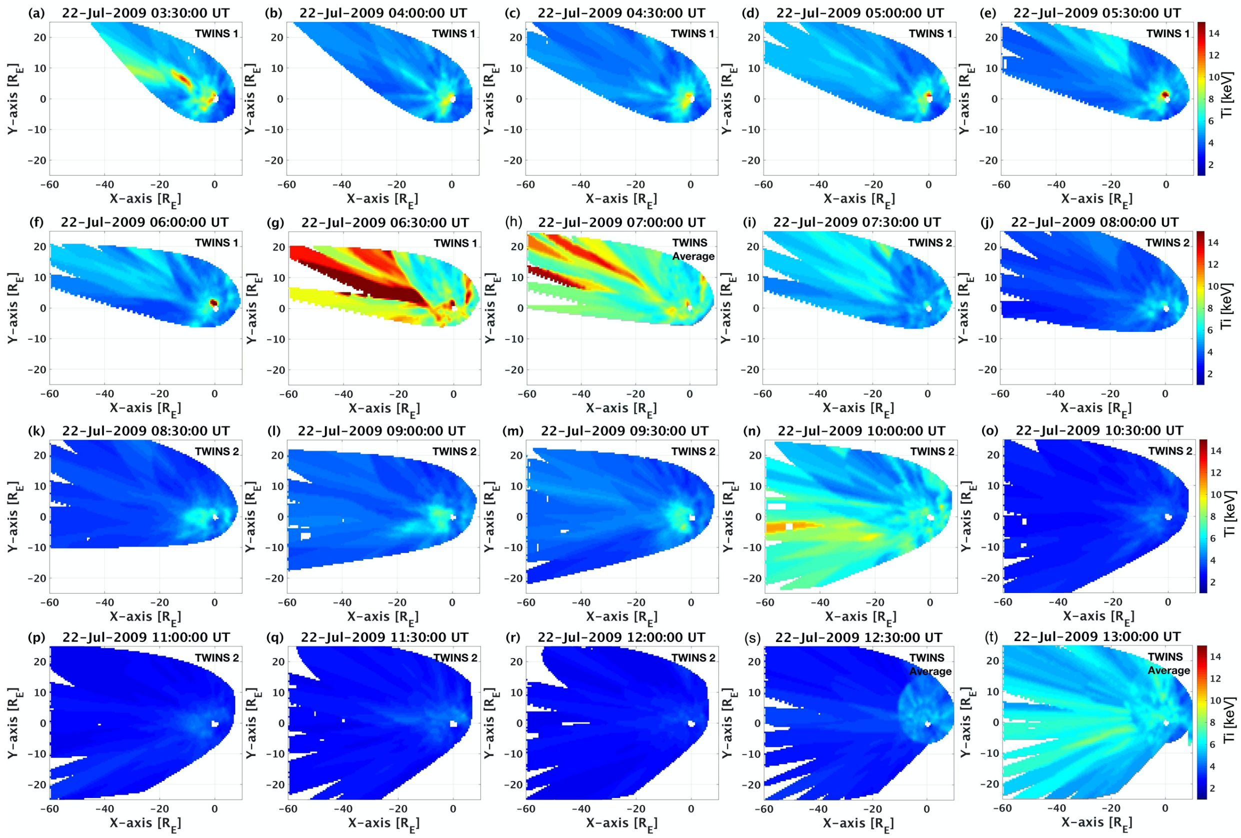

Figure 4. TWINS-derived ion temperature maps. The sequence shows a 10-minute average every 30 minutes from 3:30 UT-13:00 UT (shaded area of Fig. 3) on July 22, 2009. Each map indicates whether it is calculated from TWINS 1, TWINS 2, or an average.

We do note that the first ion temperature increase and beginning of the subsequent temperature drop occur during an interval of overlap between the two TWINS satellites, as does the final temperature recovery. The orbits of the satellites are shown in Figure 5 and the overlapping temperature maps are shown in Figure 6, including the individual maps from TWINS 1 and TWINS 2 as well as the averaged map, so that we may examine them more closely. The first overlapping interval lasts 6:30 UT-7:30 UT where TWINS 1 is descending toward perigee and TWINS 2 is ascending toward apogee. It can be seen from Figure 5 that the satellites are relatively close to each other during this interval, resulting in the similarly shaped FOVs in Figs. 6 a-d. The average temperature observed by TWINS 1 is quite a bit higher than TWINS 2 for most of this overlapping interval (Figs. 6a-c), resulting in the large peak seen in Figure 3. It is possible for in situ particle contamination to occur as the satellites are lower in their orbits, but the TWINS Lyman-alpha detectors do not indicate higher than usual counts during this interval (not shown). Since this temperature peak occurs during the peak of the storm, it is likely that TWINS 1 observes energetic particles in the inner magnetosphere that are erroneously mapped to the tail. Both of these possibilities tend to result in the large regions with high temperatures observed in Fig. 4 g-h. Rather than a region with a gradual gradient as seen in e.g. Fig. 4a, these effects yield sharp enhancements that follow the lines of the projection. Since this occurs when the satellite is low in its orbit, the projected FOV for each pixel is stretched significantly. Thus, average temperatures during intervals of satellite overlap can be erroneously high. However, TWINS 2 does also observe an increase in temperatures over this interval, just with a reduced magnitude, and the agreement in the final overlapping interval (Fig. 6d) is good. Similarly, another overlap occurs over ~ 12:10 UT – 13:30 UT (every other 10 minute interval is shown in Figs. 6e-h), now with TWINS 1 ascending toward apogee and TWINS 2 descending toward perigee. During this interval, the satellites are in quite different locations, as seen in Fig. 5, resulting in very different FOVs, as seen in Figs. 6 e-h. However, there is much better agreement in average temperature between the two satellites over most of this interval, indicating that the mappings of the increased temperatures observed at this time are mutually consistent, though the exact timing is unclear as seen in the difference between the satellites early in this interval in Fig. 6e. The takeaway from this comparison is that the timing and intensity of the temperature variations will have to be carefully considered, especially during intervals when the satellites are lower in their orbits.

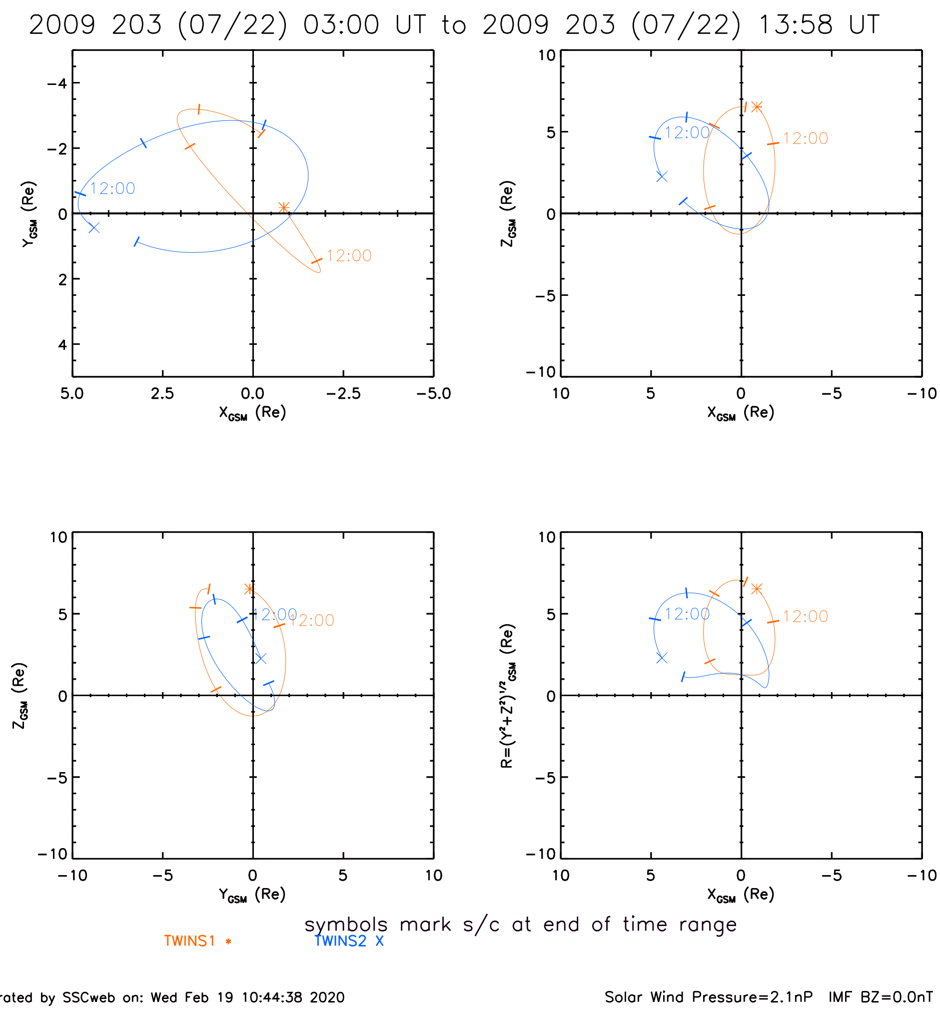

Figure 5. Orbital plots from SSCweb for TWINS 1 (red *) and TWINS 2 (blue X) for July 22, 2009 3:00 UT – 14:00 UT. Tick marks are every 3 hours and the symbols mark the location at the end of the interval.

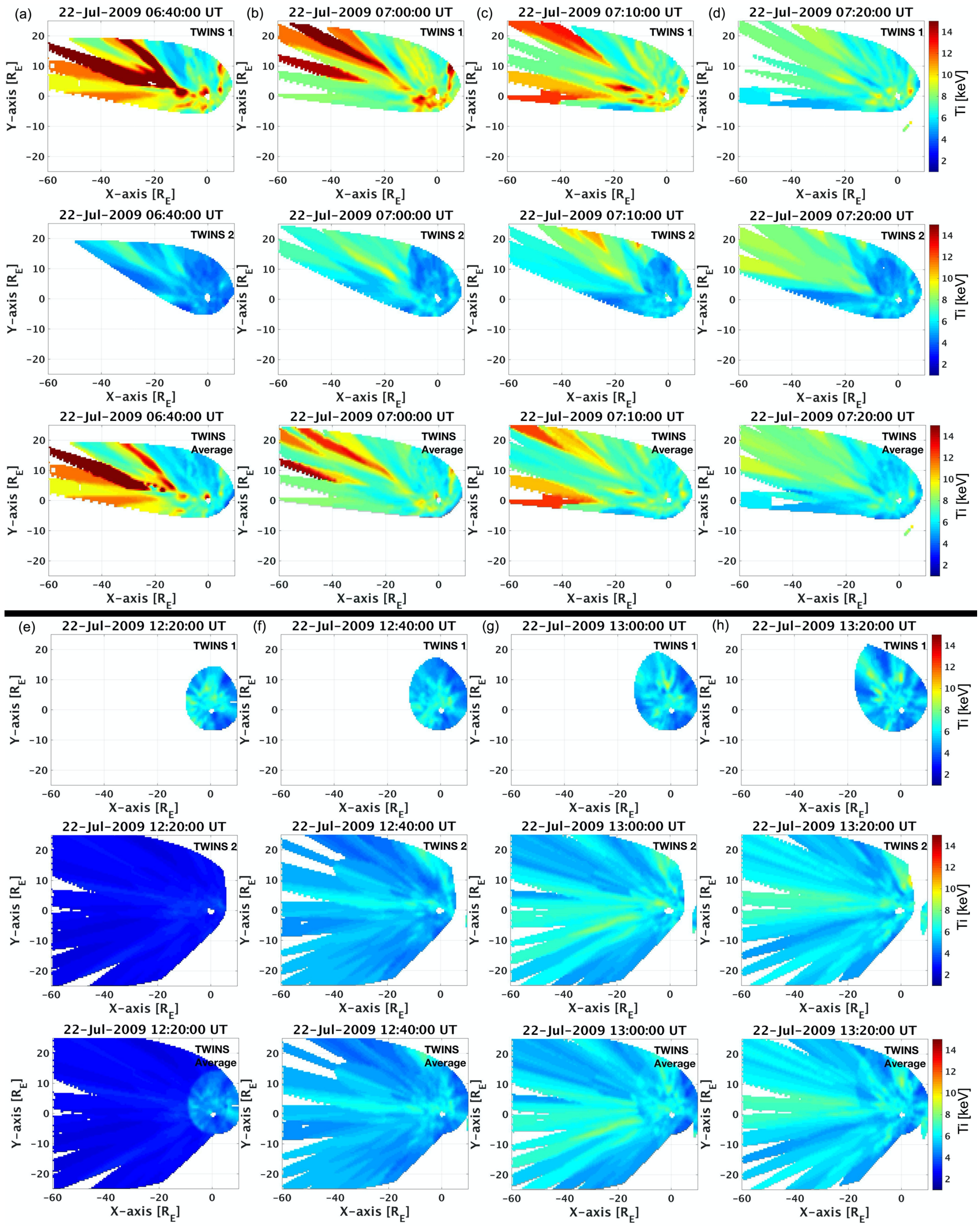

Figure 6. Ion temperature maps for TWINS 1 and TWINS 2 during intervals of overlapping coverage on July 22, 2009, including (a-d) 6:40 UT – 7:30 UT and (e-h) every other 10 minute interval over 12:20 UT-13:30 UT.

A strong or prolonged northward IMF allows energetic electrons to collect in the plasma sheet. A southward turning of the IMF B_z then triggers magnetic reconnection in the tail, resulting in the injection of hot ions from the plasma sheet to the inner magnetosphere (e.g. Iyemori, 1980; Thomsen, Borovsky, Skoug, & Smith, 2003). The trend of the plasma sheet ion temperature drop is an indication of this “clearing” of the hot ions from the plasma sheet. There are AE peaks that occur around the time of the ion temperature drops (Fig. 3) indicating substorm activity. These initial observations indicate the strength of the B_z temporal gradient is an important factor in triggering this clearing. Slow, gradual southward turning does not result in the lower temperatures. As described previously for the July 2009 storm, the second interval has a stronger temporal gradient and results in lower plasma sheet temperatures. The sharp gradients in B_z are an indication of the solar wind structure, which depends on the storm driver. The July storm was driven by a co-rotating interaction region (CIR) (Amy M. Keesee & Scime, 2015), and our preliminary survey found similar occurrences during coronal mass ejection (CME)-driven storms. Further study is needed to better understand these differences that influence the plasma sheet temperature. The strength of the IMF B_y may also play a role. Penetration of the IMF B_y into the magnetosphere enhances the cross-tail B_y, thus increasing Earthward convection. A strong IMF B_y is seen in these intervals, with a change in direction occurring at a similar time as the end of the interval of low plasma sheet temperatures. Thus, when the B_y weakens, so does the convection, enabling the plasma sheet to refill with hotter ions. We plan to conduct a more comprehensive study of the entire database, including a superposed epoch analysis as a function of storm strength and driver, in the near future to better understand these drops in plasma sheet ion temperature.

4 Conclusions

We have calculated equatorial ion temperature maps at 10-minute cadence for 90 geomagnetic storms using TWINS ENA data. This database of ion temperature maps has been made available at CDAWeb in cdf format with the necessary metadata for community use in modeling and other magnetospheric studies. As an example, we have conducted a preliminary analysis of plasma sheet ion temperature trends in relation to solar wind dynamics. We have found that a drop in ion temperatures occurs in conjunction with strong southward gradient in IMF B_z in several intervals and presented a case study of one storm. This is consistent with the hot ions being injected during a substorm triggered by the southward increase in certain cases, leaving a cooler plasma sheet behind. Further studies of this phenomenon will be conducted.

Acknowledgments, Samples, and Data

TWINS data, both ENA format (TWINSX_L1_IMAGER) and temperature maps (TWINS_M2_ENA) described in this paper, are available at https://cdaweb.gsfc.nasa.gov/index.html/.

References

Angelopoulos, V., Kennel, C. F., Kivelson, M. G., Walker, R. J., & Paschmann, G. (1992). Bursty Bulk Flows in the Inner Central Plasma Sheet. *Journal of Geophysical Research*, *97*(A4), 4027–4039.

Borovsky, J. E., Thomsen, M. F., & Elphic, R. C. (1998). The driving of the plasma sheet by the solar wind layer. *Journal of Geophysical Research*, *103*, 17,617-17,639.

Chen, M. W., Lemon, C. L., Guild, T. B., Keesee, A. M., Lui, A., Goldstein, J., … Anderson, P. C. (2015). Effects of modeled ionospheric conductance and electron loss on self-consistent ring current simulations during the 5-7 April 2010 storm. *Journal of Geophysical Research: Space Physics*, *120*, 5355–5376. https://doi.org/10.1002/2015JA021285

Elfritz, J., Keesee, A., Buzulukova, N., Fok, M.-C., & Scime, E. E. (2014). First results using TWINS-derived ion temperature boundary conditions in CRCM. *Journal of Geophysical Research*, *119*, 3345–3361. https://doi.org/10.1002/2013JA019555

Goldstein, J., & McComas, D. J. (2013). Five years of stereo magnetospheric imaging by TWINS. *Space Science Reviews*, *180*(1–4), 39–70. https://doi.org/10.1007/s11214-013-0012-8

Goldstein, J., & McComas, D. J. (2018). The Big Picture: Imaging of the Global Geospace Environment by the TWINS Mission. *Reviews of Geophysics*, *56*(1), 251–277. https://doi.org/10.1002/2017RG000583

Iyemori, T. (1980). Time Delay of the Substorm Onset from the IMF Southward Turning. *Journal of Geomagnetism and Geoelectricity*, *32*(5), 267–273. https://doi.org/10.5636/jgg.32.267

Katus, R. M., Keesee, A. M., Scime, E., & Liemohn, M. W. (2017). Storm time equatorial magnetospheric ion temperature derived from TWINS ENA flux. *Journal of Geophysical Research: Space Physics*, *122*, 3985–3996. https://doi.org/10.1002/2016JA023824

Katus, Roxanne M, Liemohn, M. W., Ionides, E., Ilie, R., & Welling, D. T. (2015). Statistical analysis of the geomagnetic response to different solar wind drivers and the dependence on storm intensity. *Journal of Geophysical Research: Space Physics*, *120*, 310–327. https://doi.org/10.1002/2014JA020712

Keesee, A. M., Elfritz, J. G., McComas, D. J., & Scime, E. E. (2012). Inner magnetosphere convection and magnetotail structure of hot ions imaged by ENA during a HSS-driven storm. *Journal of Geophysical Research*, *117*, A00L06. https://doi.org/10.1029/2011JA017319

Keesee, A., Scime, E., Zaniewski, A., & Katus, R. (2019). 2D Ion Temperature Maps from TWINS ENA data: IDL scripts. UNH Scholars' Repository. https://doi.org/https://dx.doi.org/10.34051/c/2019.1

Keesee, A M, Chen, M. W., Scime, E. E., & Lui, A. T. Y. (2014). Regions of ion energization observed during the Galaxy-15 substorm with TWINS. *Journal of Geophysical Research: Space Physics*, *119*, 8274–8287. https://doi.org/10.1002/2014JA020466

Keesee, Amy M., & Scime, E. E. (2015). Database of ion temperature maps during geomagnetic storms. *Earth and Space Science*, *2*, 39–46. https://doi.org/10.1002/2014EA000061

Keesee, Amy M., Scime, E., & Moldwin, M. B. (2008). Remote measurements of ion temperatures in the terrestrial magnetotail. *Journal of Geophysical Research*, *113*, A00A03. https://doi.org/10.1029/2008JA013130

McComas, D. J., Allegrini, F., Baldonado, J., Blake, B., Brandt, P. C., Burch, J., … Zoennchen, J. (2009). The Two Wide-angle Imaging Neutral-atom Spectrometers (TWINS) NASA Mission-of-Opportunity. *Space Science Reviews*, *142*(1–4), 157–231. https://doi.org/10.1007/s11214-008-9467-4

Ozeke, L. G., & Mann, I. R. (2008). Energization of radiation belt electrons by ring current ion driven ULF waves. *Journal of Geophysical Research: Space Physics*, *113*(2), 4–11. https://doi.org/10.1029/2007JA012468

Scime, E. E., Keesee, A. M., Jahn, J.-M., Kline, J. L., Pollock, C. J., & Thomsen, M. (2002). Remote ion temperature measurements of Earth's magnetosphere: Medium energy neutral atom (MENA) images. *Geophysical Research Letters*, *29*(10), 1438. Retrieved from http://www.agu.org/pubs/crossref/2002/2001GL013994.shtml

Spence, H. E., & Kivelson, M. (1993). Contributions of the low-latitude boundary layer to the finite width magnetotail convection model. *Journal of Geophysical Research*, *98*, 15487–15496. Retrieved from http://www.igpp.ucla.edu/people/mkivelson/Publications/144-93JA01531.pdf

Takahashi, N., Seki, K., Amano, T., Miyoshi, Y., & Yamakawa, T. (2019). Excitation of storm-time Pc5 ULF waves by ring current ions based on the drift-kinetic simulation. *Geophysical Research Letters*, 1911–1918. https://doi.org/10.1029/2018gl081573

Thomsen, M. F., Borovsky, J. E., Skoug, R. M., & Smith, C. W. (2003). Delivery of cold, dense plasma sheet material into the near-Earth region. *Journal of Geophysical Research*, *108*(A4), 1151. https://doi.org/10.1029/2002JA009544

Tsyganenko, N. A., & Mukai, T. (2003). Tail plasma sheet models derived from Geotail particle data. *Journal of Geophysical Research*, *108*(A3), 1–15. https://doi.org/10.1029/2002JA009707

Wiltberger, M., Merkin, V., Lyon, J. G., & Ohtani, S. (2015). High-resolution global magnetohydrodynamic simulation of bursty bulk flows. *Journal of Geophysical Research : Space Physics*, *120*, 4555–4566. https://doi.org/10.1002/2015JA021080

Zhao, H., Baker, D. N., Li, X., Jaynes, A. N., & Kanekal, S. G. (2019). The Effects of Geomagnetic Storms and Solar Wind Conditions on the Ultrarelativistic Electron Flux Enhancements. *Journal of Geophysical Research: Space Physics*, *124*(3), 1948–1965. https://doi.org/10.1029/2018JA026257

Storm Start Date	Peak Dst [nT]
07/21/2009	-83
02/14/2010	-59
03/12/2010	-30
04/05/2010	-81
05/01/2010	-71
05/28/2010	-80
08/03/2010	-74
10/10/2010	-75
02/04/2011	-63
02/28/2011	-88
03/10/2011	-83
05/27/2011	-80
08/05/2011	-115
09/08/2011	-75
09/16/2011	-72
09/25/2011	-118
09/27/2011	-68
10/24/2011	-147
10/31/2011	-66
01/22/2012	-71
01/24/2012	-75
02/14/2012	-67
03/06/2012	-88
03/08/2012	-145
03/14/2012	-88
03/27/2012	-68
04/23/2012	-120
06/16/2012	-86
07/14/2012	-139
07/18/2012	-80
09/02/2012	-76
09/30/2012	-122
10/07/2012	-99
10/08/2012	-109
10/13/2012	-90
10/31/2012	-65
11/13/2012	-108
03/16/2013	-132
03/28/2013	-59
04/30/2013	-72
05/31/2013	-124
06/06/2013	-78

06/28/2013	-102
07/05/2013	-87
07/13/2013	-81
10/01/2013	-72
10/08/2013	-69
11/08/2013	-80
11/10/2013	-68
12/07/2013	-66
02/18/2014	-119
02/21/2014	-64
03/02/2014	-52
04/11/2014	-87
04/29/2014	-67
05/02/2014	-47
08/26/2014	-79
09/13/2014	-88
01/03/2015	-71
01/06/2015	-99
02/17/2015	-64
03/17/2015	-223
03/19/2015	-88
04/09/2015	-75
04/15/2015	-79
05/12/2015	-76
06/07/2015	-73
06/21/2015	-204
06/24/2015	-86
07/04/2015	-67
07/12/2015	-61
07/22/2015	-63
08/14/2015	-84
08/26/2015	-92
08/26/2015	-89
09/08/2015	-98
09/10/2015	-81
09/19/2015	-75
10/06/2015	-93
10/06/2015	-124
11/06/2015	-89
12/19/2015	-155
12/31/2015	-110
01/19/2016	-93
03/05/2016	-98
05/07/2016	-88
08/23/2016	-74

09/28/2016	-66
10/12/2016	-103
10/28/2016	-64
03/01/2017	-61
03/26/2017	-74
05/27/2017	-125
07/15/2017	-72
07/16/2017	-61
09/07/2017	-124
09/08/2017	-109
09/27/2017	-55
11/07/2017	-74